

RESEARCH ARTICLE

10.1002/2017JF004221

Key Points:

- The presence of large immobile boulders significantly influences the flow and turbulence field in the vicinity of submerged boulders
- The boulder concentration plays an important role in forming skimming to isolated roughness flows and predicting bed load transport rates
- The bed load transport rate will be underestimated when using the reach-averaged shear stress, compared with that based on local shear stress

Supporting Information:

- Supporting Information S1
- Movie S1

Correspondence to:

Y. Liu,
yanliu12@mails.tsinghua.edu.cn

Citation:

Fang, H. W., Liu, Y., & Stoesser, T. (2017). Influence of boulder concentration on turbulence and sediment transport in open-channel flow over submerged boulders. *Journal of Geophysical Research: Earth Surface*, 122, 2392–2410. <https://doi.org/10.1002/2017JF004221>


Received 17 JAN 2017

Accepted 6 NOV 2017

Accepted article online 16 NOV 2017

Published online 19 DEC 2017

Influence of Boulder Concentration on Turbulence and Sediment Transport in Open-Channel Flow Over Submerged Boulders

H. W. Fang¹, Y. Liu¹, and T. Stoesser² 

¹Department of Hydraulic Engineering, Tsinghua University, Beijing, China, ²School of Civil Engineering, Cardiff University, Cardiff, UK

Abstract In this paper the effects of boulder concentration on hydrodynamics and local and reach-averaged sediment transport properties with a flow over submerged boulder arrays are investigated. Four numerical simulations are performed in which the boulders' streamwise spacings are varied. Statistics of near-bed velocity, Reynolds shear stresses, and turbulent events are collected and used to predict bed load transport rates. The results demonstrate that the presence of boulders at various interboulder spacings altered the flow field in their vicinity causing (1) flow deceleration, wake formation, and vortex shedding; (2) enhanced outward and inward interaction turbulence events downstream of the boulders; and (3) a redistribution of the local bed shear stress around the boulder consisting of pockets of high and low bed shear stresses. The spatial variety of the predicted bed load transport rate q_b , based on local bed shear stress is visualized and is shown to depend greatly on the boulder concentration. Quantitative bed load transport calculations demonstrate that the reach-averaged bed load transport rate may be overestimated by up to 25 times when including the form-drag-generated shear stress of the immobile boulders in the chosen bed load formula. Further, the reach-averaged bed load transport rate may be underestimated by 11% if the local variability of the bed shear stress is not accounted for. Finally, it is shown that for the small-spaced boulder array, the bed load transport rates should no longer be predicted using a normal distribution with standard deviation of the shear stress distribution σ .

1. Introduction

Large, immobile boulders are common in steep, mountain streams and can significantly alter local flow fields, turbulent structures, sediment transport rates, and aquatic habitats (e.g., Bathurst, 1987; Dey et al., 2011; Rickenmann, 2001; Tsakiris et al., 2014; Yager et al., 2007). The roughness of a streambed occupied by large boulders may be classified via their flow regime, i.e., isolated, wake interference or skimming flow regimes (Papanicolaou et al., 2001; Papanicolaou et al., 2002). The boulder-to-boulder spacing or boulder concentration is usually used to distinguish between the three flow regimes. For example, Papanicolaou et al. (2001) in their flume experiments used a boulder spacing of 6, 2, and 1 times the boulder diameter to study isolated, wake interference and skimming flow regimes, respectively. Ferro (1999) stated that the channel flow is in the skimming flow regime when the boulder concentration is larger than 50%, or in other words, when 50% of the channel bed is occupied by boulders.

Attempts to account for the impact of large boulders of the three flow regimes on bed load transport included modification of the flow resistance (total shear stress) (Canovaro et al., 2007; Ferro, 1999; Ferro, 2003) or usage of the critical shear stress in the bed load transport rate equations (Bathurst, 1987, 2007; Lenzi et al., 2006; Mao et al., 2008). Flume experiments have found that the flow resistance is a function of the boulder concentration (Bathurst et al., 1981; Canovaro et al., 2007; Ferro, 1999). Within the isolated flow regime, the flow resistance is proportional to the number of boulders, while within wake interference and skimming flow regimes, the flow resistance can no longer be given in terms the number of boulders (Canovaro et al., 2007). Field studies and experiments have confirmed that the critical shear stress of a wide range of sediment sizes (including large boulders) is usually much higher than that of a narrow range of sediment sizes (Bathurst, 1987, 2007; Lenzi et al., 2006; Mao et al., 2008). Several explanations are proposed including (a) immobile boulders exert drag on the flow, reducing the shear stress available to transport finer sediments (e.g., Buffington & Montgomery, 1997; Patel et al., 2013; Xu et al., 2008); (b) the immobile boulders provide shelter for mobile gravel from high shear stresses (e.g., Wiberg & Smith, 1991); (c) an armor layer

forms by the coarser sediments and limits sediment supply of finer sediments (e.g., Bathurst, 2007); or (d) the immobile boulders produce a low, uniform velocity profile close to the bed and reduce near-bed peak turbulence intensity when relative roughness increases (e.g., Lamb et al., 2008; Recking, 2009).

With regard to bed load transport in streams with large boulders it has been recognized that boulders significantly increase spatial variability of the flow field and turbulence intensities at the patch scale (Dey et al., 2011; Ozgoren et al., 2013; Parker, 2008; Shamloo et al., 2001). In terms of the mean velocity field, boulder wakes form as a result of the recirculation zones downstream of submerged boulders. Large-scale coherent flow structures dominate the instantaneous and local flow in the vicinity of boulders (Ferro, 2003; Hajimirzaie et al., 2014; Strom & Papanicolaou, 2007; Tsakiris et al., 2014). Such structures include tip vortices created by flow separation at the crest (Hajimirzaie et al., 2014), and near-bed horseshoe vortices just upstream of the boulder (Tsutsui, 2008). Moreover, coherent flow structures enhance significantly turbulence levels and local turbulent shear stresses and alter the vertical turbulence intensity profiles (Hajimirzaie et al., 2014).

Although flow patterns over large boulders have received considerable attention, there are still difficulties of quantifying bed load transport under consideration of the noneffective shear stress (in the form of the pressure or form drag) due to the large immobile boulders. One available method is to calculate the skin shear stress on the mobile bed and the form drag individually via a form drag formula. This method has been applied by several researchers in their studies of predicting flow velocities and bed load transport rates in channels with large roughness elements (Ghilardi et al., 2014; Nitsche et al., 2012; Scheingross et al., 2013; Yager et al., 2007, 2012). One of the challenges of this method is to determine the empirical drag coefficient C_m for the mobile sediments. Different constant values have been used by researchers, such as $C_m = 0.047$ (Yager et al., 2007), $C_m = 0.44$ (Yager et al., 2012), and $C_m = 0.12\sim 1.27$ (Scheingross et al., 2013). These values, attained via calibration, appear to vary within approximately 2 orders of magnitude. Several other methods of partitioning the total shear stress included various other assumptions. For example, Canovaro et al. (2007) assumed the skin shear stress to be linearly correlated with the boulder concentration. Thus, the skin shear stress for a given boulder concentration is obtained by interpolation of the skin shear stress between a highest (100%) and lowest (0%) boulder concentration, which are measured. Papanicolaou et al. (2012) assumed that the velocity defect law is valid in the outer flow layer ($z/H > 0.2$) to enable the calculation of skin shear stress and form drag by a boundary characteristics method. These assumptions are necessary to compensate for the lack of knowledge of the real skin shear stress and may cause large inaccuracies in the prediction of bed load transport rates using shear stress-based bed load transport formulae (Ferguson, 2003).

In addition to the difficulty of partitioning the total shear stress into skin friction and form drag, the local skin shear stress is also difficult to measure and/or predict. Segura and Pitlick (2015) and Monsalve et al. (2016) used a 2-D flow model to predict the spatially varying shear stress distribution, based on the (empirical) drag coefficient C_d and the depth-averaged flow velocity. Their results show the ability to reproduce the water surface elevation as compared to the observed data, and they successfully predict the shear stress distribution in a natural river. However, there are differences of the local and cross-section-averaged velocities between model predictions and observed data, which may lead to inaccurate predictions of local shear stress in their model. Furthermore, the shape of the vertical velocity profile of the flow over submerged boulders may attain various shapes, such as S-shape, log-law shape, and linear shape (Byrd et al., 2000; Ferro, 2003). Even at the same depth-averaged flow velocity, the near bed velocities and near bed shear stresses could differ significantly, suggesting the necessity of carrying out 3-D numerical simulations to predict the local bed shear stress between the boulders.

In this study, large-eddy simulations of flow over arrays of boulders at various interboulder spacings are performed. The large-eddy simulation (LES) results are analyzed in order to answer the following questions: (1) What is the spatial variability in near-bed turbulence, shear stresses, and sediment movement over boulder arrays? (2) How does the boulder-to-boulder spacing influence local sediment transport? (3) How accurate are calculations of sediment transport of flow over boulder arrays based on local-scale parameters and reach-scale parameters? The paper is organized as follows: Section 2 provides details of the numerical methods to predict flow and sediment transport. Section 3 presents simulation data and calculations in the form of figures and brief descriptions thereof. Section 4 discusses the results in the context of sediment transport predictions. The paper finishes with conclusions in section 5.

2. Methods

2.1. Large-Eddy Simulations

In this study, the in-house code Hydro3D is employed for the large-eddy simulation (LES). Hydro3D has been validated for and applied to several flows of similar complexity to those reported here (Bomminayuni & Stoesser, 2011; Bai et al., 2013; Fraga Bugallo & Stoesser, 2016; Fraga Bugallo et al., 2016; Kara et al., 2012; Kim et al., 2013; Kara, Stoesser, & McSherry, 2015; Kara, Stoesser, & Sturm, 2015; Kim & Stoesser, 2011). The code is based on a finite difference method on a staggered Cartesian grid. The filtered Navier-Stokes equations for incompressible, unsteady, and viscous flow are solved as given below:

$$\frac{\partial u_i}{\partial x_i} = 0 \quad (1)$$

$$\frac{\partial u_i}{\partial t} + \frac{\partial u_i u_j}{\partial x_j} = -\frac{\partial p}{\partial x_i} + \frac{\partial (2\nu S_{ij})}{\partial x_j} - \frac{\partial \tau_{ij}}{\partial x_j} \quad (2)$$

where u_i and u_j are spatially resolved velocity vectors (i and $j = 1, 2,$ and 3 represent $x, y,$ and z axis directions, respectively), and similarly, x_i and x_j represent the spatial-location vectors in the three directions; p is the spatially resolved pressure divided by the flow density, ν is the kinematic viscosity, and S_{ij} denotes the filtered strain rate tensor and is calculated as $S_{ij} = 1/2(\partial u_i/\partial x_j + \partial u_j/\partial x_i)$. The subgrid-scale (SGS) stress τ_{ij} SGS is defined as $\tau_{ij} = -2\nu_t S_{ij}$. In this study, the wall-adapting local eddy viscosity proposed by Nicoud and Ducros (1999) is used to calculate the eddy viscosity, ν_t , and model the SGS stress.

The convection and diffusion terms in the Navier-Stokes equations are approximated by fourth-order accurate central differences. An explicit three-step Runge-Kutta scheme is used to integrate the equations in time, providing second-order accuracy. A fractional step method is employed; i.e., within the time step convection and diffusion terms are solved explicitly first in a predictor step, which is then followed by a corrector step during which the pressure and divergence-free-velocity fields are obtained through a Poisson equation. The latter is solved iteratively through a multigrid procedure. Details of the code are reported in Cevheri et al. (2016).

2.2. Computational Setups

Three numerical simulations of flow over an array of staggered boulders, of diameter D_c , with different streamwise boulder-to-boulder spacing λ are performed. The computational domain, for each simulation, spans $10 D_c$ in the streamwise direction, $6.93 D_c$ in the spanwise direction, and $3.83 D_c$ in the vertical direction, and the domains for the three simulations with boulders are presented in Figure 1. In addition, a fourth simulation is performed without boulders. For all four simulations the channel bed is artificially roughened by one layer of closely packed spheres of diameter d . The virtual bed elevation ($z/D_c = 0$) is set at the top crest of the bed spheres, which indicates that the bed spheres are placed at the region from $z/D_c = -0.33$ to $z/D_c = 0.0$ and the water depth, H , is $H/D_c = 3.5$. Different numbers of big boulders (N_b) are placed on top of the bed spheres with streamwise spacing of infinite (no-boulder simulation), $10 D_c$ (large spacing), $5 D_c$ (medium spacing), and $2 D_c$ (small spacing). The spanwise spacing is maintained at $3.46 D_c$. The boulder concentrations, Γ , defined as the projected area of the boulder A_b divided by the total bed area A_t , are 0.00%, 2.27%, 4.53%, and 11.33% for the infinite-, large-, medium-, and small-spacing simulations, respectively. The ratio of the big-boulder diameter D_c to the bed-sphere diameter d is 3. In order to investigate and reveal directly the effect of boulder-to-boulder spacing on hydrodynamics and sediment transport of flow over boulder arrays, the water depth and the bulk velocity are maintained constant. Hence, the relative submergence of the big boulder, H/D_c , which is a key parameter affecting the flow around obstacles, is thus kept constant between runs and differences in the hydrodynamics, and bed load transport predictions between the different runs are caused solely by the boulder concentration. All simulations are carried out at a relatively high Reynolds number of $Re = 150,500$, based on the water depth, the bulk velocity, and the kinematic viscosity. The dimensionless flow conditions of the four LESs are provided in Table 1.

The setup of the large-spacing simulation is similar to that of a flume experiment by Papanicolaou et al. (2012) to allow for the validation of the numerical method. The experiment was conducted in a 21 m long, 0.91 m wide, and 0.53 m deep flume. A rough, permeable bed was constructed atop the flume bottom by arranging three layers of spherical glass particles with diameter $d = 19.1$ mm in a hexagonal pattern. An array of

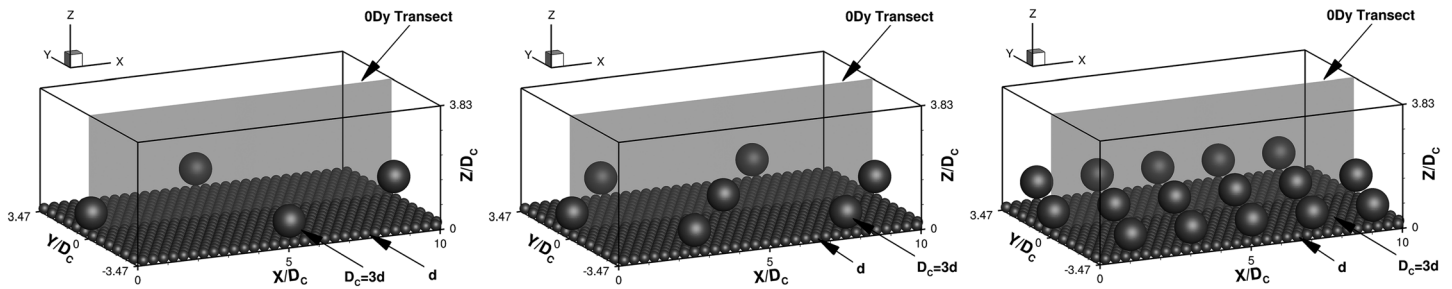


Figure 1. Computational domains for simulations with $\lambda = 10 D_c$, $5 D_c$, and $2 D_c$.

spherical boulders with diameter $D_c = 55$ mm was rigidly mounted atop the rough bed with diagonal spacing of $6 D_c$, which is the same to the diagonal spacing of our large-spacing simulation. The dimensional flow conditions (using the viscosity, ν , of water) of the experiment and the large-spacing simulation are provided in Table 2. The LES is an upscaled Reynolds model of the experiment to minimize round-off errors and to optimize the grid spacing. The predicted reach-averaged shear velocity, u_* , computed from the time-averaged pressure gradient dp/dx as $u_* = (dp/dx)^{0.5} H^{0.5}$, normalized with the bulk velocity u_*/U_{bulk} , of the LES is 0.101, and it agrees very well with the experimental value, which is $u_*/U_{\text{bulk}} = 0.097$. The validity of the large-spacing LES including proof of the adequacy of the domain size and the grid spacing is reported in Liu et al. (2017).

Periodic boundary conditions are applied in the streamwise and spanwise directions, mimicking fully developed flow in both these directions. The water surface is treated as a frictionless rigid lid at which the free-slip condition is applied. The use of the rigid lid condition is deemed a reasonable treatment given the relatively low Froude number and the experimentally observed relatively flat water surface. The no-slip condition is applied on the surfaces of the spheres and boulders and at the bottom wall. In order to achieve the no-slip condition on the spheres, a refined version (Kara, Stoesser, Sturm, & Mulahasan, 2015) of the direct-forcing immersed-boundary method proposed by Uhlmann (2005) is used.

A grid sensitivity study of three grids using $600 \times 480 \times 230$ (fine mesh), $480 \times 384 \times 184$ (medium mesh), and $360 \times 288 \times 138$ (coarse mesh) grid points in the x , y , and z directions, respectively, was carried out and reported in a previous paper (Liu et al., 2017). It has been shown that the maximum difference in terms of time-averaged velocities between the fine and medium mesh is only less than 2% of U_{bulk} , while differences between the medium mesh and coarse velocities are greater than 20% of U_{bulk} . Hence, the finest grid using $600 \times 480 \times 230$ grid points is chosen to carry out the large-eddy simulations for all the other runs. The grid spacing is $\Delta x^+ \approx \Delta z^+ \approx 32$, $\Delta y^+ \approx 28$ in terms of wall units, and is based on the global shear velocity (which includes the form drag of the large boulders). Each simulation is initially run for 10 flow-throughs (1 flow-through equals approximately 0.7 s in physical time) to establish fully developed turbulence and is then continued for another 60 flow-throughs while collecting first- and second-order turbulence statistics.

2.3. Quadrant Analysis

In order to better understand the role of coherent flow structures in transporting sediments for submerged-boulder-dominated flows, quadrant analyses of the velocity fluctuations are performed (e.g., Dey et al., 2011). Time series of instantaneous velocities are collected at 60 selected near-bed locations in the $0 D_y$ transect

Table 1
Flow Conditions of the Four LES Runs

| Run | λ/D_c | N_B | Γ | U_{bulk} (m/s) | H/D_c | Re (UH/ ν) | D_c/d | u^*/U_{bulk} |
|------------------|---------------|-------|----------|-------------------------|---------|-------------------|---------|-----------------------|
| Infinite spacing | – | 0 | 0.00% | 1 | 3.5 | 150,500 | 3 | 0.078 |
| Large spacing | 10 | 2 | 2.27% | 1 | 3.5 | 150,500 | 3 | 0.101 |
| Medium spacing | 5 | 4 | 4.53% | 1 | 3.5 | 150,500 | 3 | 0.135 |
| Small spacing | 2 | 10 | 11.33% | 1 | 3.5 | 150,500 | 3 | 0.141 |

Table 2

Conditions of the LES Run and the Experimental Setup of Papanicolaou et al. (2012).

| Run | H (m) | U_{bulk} (m/s) | D_c (m) | d (m) | ν (m^2/s) | Re (-) |
|------------|---------|-------------------------|-----------|---------|---------------------------------|----------|
| LES | 3.36 | 1 | 0.960 | 0.320 | 2.23×10^{-5} | 150,500 |
| Experiment | 0.193 | 0.78 | 0.055 | 0.019 | 1.0×10^{-6} | 150,500 |

(i.e., $y/D_c = 0$ in Figure 1). The sample locations have a uniform x distribution with a deviation of $1/6 D_c$ (i.e., $x/D_c = 1/6, 1/3, \dots, 10$), a constant y value, $y/D_c = 0$, and a constant z value, $z/D_c = 0.1$, above the bed spheres. The time step of the instantaneous velocity is approximately 0.00035 s. Instantaneous velocity data points (50,000) are collected; thus, the total duration of the event is approximately 17.5 s or 25 flow-throughs. The streamwise and vertical velocity fluctuations are calculated as

$$u' = u - \langle u \rangle \quad (3)$$

$$w' = w - \langle w \rangle \quad (4)$$

where u and w are the instantaneous streamwise and vertical velocities and $\langle u \rangle$ and $\langle w \rangle$ are the time-averaged streamwise and vertical velocities. The joint distribution of u' and w' is divided into four quadrants: bursts ($u' < 0, w' > 0$), sweeps ($u' > 0, w' < 0$), inward interactions ($u' < 0, w' < 0$), and outward interactions ($u' > 0, w' > 0$). Among the four quadrants, duration of the bursts events is suggested to be associated with the sediment entrainment flux from the bed (Cao, 1997). Therefore, the interval between the j th and $(j + 1)$ th burst event, T_{Bj} , is calculated during the 17.5 s period. By averaging all the burst event intervals, an average

burst event period, $T_B = \sum_{j=1}^{j_t-1} T_{Bj}/j_t$, in which j_t is the total number of burst events, is obtained. In order to allow

comparisons with other investigations, the burst event period is nondimensionalized with the viscous time-scale, $Tb^+ = Tb/(v/u_*^2)$, where u_* is the reach-averaged shear velocity shown in Table 1 and ν is the kinematic viscosity.

The joint-distribution quadrant fractions ($S_{i,H}$) are given by

$$S_{i,H} = \frac{1}{T u' w'_0} \int_0^T u'(x, z, t) w'(x, z, t) l_{i,H}(u', w', t) dt \quad (5)$$

where T is the total duration of the instantaneous velocity data set and i is the quadrant from 1 to 4, H (here $H = 0$) is the hole size. $l_{i,H}$ is a conditional function that determines if the u' and w' at a given time are within quadrant i and are given by

$$l_{i,H}(u', w', t) = \begin{cases} 1 & \text{if in quadrant } i \text{ and if } \frac{|u' w'|}{|u' w'_0|} \geq H \\ 0 & \text{otherwise} \end{cases} \quad (6)$$

The total proportion of each turbulent event, $P_{i,H}$, is calculated as

$$P_{i,H} = \frac{\int_0^T |u'(x, z, t) w'(x, z, t)| l_{i,H}(u', w', t) dt}{\int_0^T |u'(x, z, t) w'(x, z, t)| dt} \quad (7)$$

where the sum of $P_{i,H}$ for the whole turbulent event is 1. $S_{i,H}$ represents the contribution of each turbulent event to the total Reynolds shear stress, and $P_{i,H}$ denotes the frequency of each turbulent event.

2.4. Sediment Transport Calculations

In order to reveal directly the impact of boulder concentration on local sediment transport, the bed load transport rate is predicted based on the mean LES-predicted flow field. Three formulae to predict bed load transport rate are considered, which are (1) Fernandez Luque and Van Beek formula (FLVB) (Fernandez Luque & Van Beek, 1976), (2) Yager's modified FLVB formula (Yager et al., 2007), and (3) a modified FLVB formula based on the findings of this study. The three formulae are as follows:

The original FLVB formula reads

$$q_s^* = 5.7(\tau_t^* - \tau_{ct}^*)^{1.5} \quad (8)$$

where q_s^* is the dimensionless bed load rate, τ_t^* is the dimensionless reach-averaged total bed shear stress, and τ_{ct}^* is the dimensionless critical bed shear stress. The q_s^* , τ_t^* , and τ_{ct}^* are given, respectively, as

$$q_s^* = \frac{q_s}{\left[(\rho_s / \rho - 1) g d_{\text{avg}}^3 \right]^{0.5}} \quad (9)$$

$$\tau_t^* = \frac{\tau_t}{(\rho_s - \rho) g d_{\text{avg}}} \quad (10)$$

$$\tau_{ct}^* = \frac{\tau_{ct}}{(\rho_s - \rho) g d_{\text{avg}}} \quad (11)$$

where q_s is the bed load rate, τ_t is the reach-averaged total bed shear stress, τ_{ct} is the critical bed-shear stress, and ρ_s and ρ are the densities of sediment and water, respectively. The d_{avg} is the weighed-averaged sediment diameter calculated by $d_{\text{avg}} = \frac{N_d}{N_{Dc} + N_d} d + \frac{N_{Dc}}{N_{Dc} + N_d} D_c$, where N_d and N_{Dc} are the total numbers of the bed spheres and boulders, respectively.

Yager et al. (2007) made three modifications to the FLVB formula, as they (1) replaced the dimensionless reach-averaged total bed shear stress τ_t^* with the dimensionless reach-averaged bed shear stress of the mobile sediment τ_m^* , (2) used the median mobile grain size rather than the median grain size of the bed to calculate the critical bed shear stress τ_{cm}^* , and (3) considered sediment transport rate only on the area occupied by the mobile sediment, A_m . Hence, Yager et al.'s modified FLVB formula reads

$$q_s^* = 5.7(\tau_m^* - \tau_{cm}^*)^{1.5} \frac{A_m}{A_t} \quad (12)$$

where A_t is the total bed area. Similar to equations (10) and (11), τ_m^* and τ_{cm}^* can be calculated using τ_m and τ_{cm} by multiplying with $(\rho_s - \rho)gd$, where d is the mobile sediment diameter. The τ_m and τ_{cm} are the reach-averaged bed shear stress on the mobile sediment and the mean critical bed shear stress, respectively.

In both equations (8) and (12), the main parameters of influence for calculating the sediment transport rate are reach-averaged variables. However, as reported by Papanicolaou et al. (2012), the local bed shear stress could be up to 1.5 times greater than the reach-averaged bed shear stress, and hence, local bed load transport may be underestimated significantly by the original FLVB equation. With the aim of taking the spatial variability of the bed shear stress into consideration, equation (12) is further modified by (1) using the local bed shear stress acting on the mobile sediments τ_{ml} instead of the reach-averaged shear stress τ_m and (2) integrating the local bed load transport rate over the bed area of mobile sediments instead of using A_m/A_t . This modification is similar to those studies incorporating shear stress distributions into sediment transport equations (Monsalve et al., 2016; Segura & Pitlick, 2015; Yager & Schmeckle, 2013). The FLVB formula is thus modified as

$$q_s^* = \int_{A_m} q_{sl}^* dA \quad (13)$$

in which

$$q_{sl}^* = 5.7(\tau_{ml}^* - \tau_{mcl}^*)^{1.5} \quad \text{if } \tau_{ml}^* \geq \tau_{mcl}^* \\ q_{sl}^* = 0 \quad \text{otherwise} \quad (14)$$

where the subscript l stands for "local." Bed load rates from equations (8), (12), and (13) are computed and compared to reveal the relative accuracy of the three formulas in predicting bed load transport rates.

In this study the local bed shear stress τ_{ml} is approximated by the time-averaged primary Reynolds shear stress at an elevation $z/D_c = 0.1$ (5.5 mm above the bed spheres):

$$\tau_{ml} = \tau_{Rl} = -\rho \langle u'w' \rangle \Big|_{z/D_c=0.1} \quad (15)$$

The reach-averaged bed shear stress τ_m is obtained by integrating τ_{ml} over the area occupied by bed spheres, A_m , as

$$\tau_m = \int_{A_m} \tau_{ml} dA \quad (16)$$

The reach-averaged total bed shear stress τ_t is calculated from the time-averaged pressure gradient dp/dx as

$$\tau_t = (dp/dx)H \quad (17)$$

In terms of the critical shear stress, $\tau_{cml}^* = \tau_{cm}^* = \tau_{ct}^* = 0.0085$ is used as suggested by Papanicolaou et al. (2012) and this is based on the diameter of the bed spheres of $d = 19.1$ mm. The value of the critical shear stress, 0.0085, is much smaller than those for natural gravel bed rivers, e.g., $\tau_c^* = 0.045$ (Buffington & Montgomery, 1997). However, this value had been obtained by Papanicolaou et al. (2012) from their laboratory experiments, in which mobile sediment particles with $d = 19.1$ mm were placed atop a flat, nonerodible, rough, porous bed consisting of glass beads with the same diameter (Papanicolaou et al., 2012). The so-obtained value closely matched the one obtained by Strom et al. (2004) for mobile particles with diameter $d = 8$ mm atop a flat rough porous bed made of well-packed identical particles with $d = 8$ mm. Strong subsurface flow through the porous bed, significant protrusion of individual mobile sediments into the flow or smooth, perfectly spherical and very smooth sphere surface of the sediment and the rough bed may all be responsible for the smaller critical shear stress in comparison with the one obtained for less-porous, nonspherical, rougher river beds/sediments. Since the current study is only interested in the effect of boulder concentration on sediment transport rates, the measured critical shear stress of Papanicolaou et al. (2012) is used in this study.

3. Results

3.1. Time-Averaged Flow and Validation

The simulations of the large-spacing boulder have been validated previously, and the accuracy of the LES in terms of first- and second-order statistics as well as adequacy of domain and grid sizes have been confirmed (Liu et al., 2017). The validation entailed comparisons of LES-predicted time-averaged streamwise velocities and turbulence intensities with experimental data from Papanicolaou et al. (2012), some of which are repeated here to highlight the credibility of the LESs. Figures 2 and 3 present computed and experimentally obtained profiles of the time-averaged streamwise velocity, $\langle u \rangle$ (Figure 2), and turbulence intensity, $\text{rms}(u')$ (Figure 3), at 10 selected locations from $0 D_x$ to $9 D_x$ along the boulder's centerline denoted $0 D_y$ transect, which is where the velocity measurements were carried out.

The presence of the boulder creates a recirculation zone downstream of the boulder followed by a wake, which is characterized by low velocities below the boulder crest and thus yields a boundary layer flow that is only recovering very slowly downstream of the recirculation zone. The streamwise velocity below the boulder's crest, e.g., below $z/D_c = 1.0$, is strongly decelerated both upstream and downstream of the boulder, especially near the bed. There is only a minor discrepancy in the streamwise velocity immediately downstream of the boulder near the bed at $x/D_c = 1.0$. The LES overpredicts somewhat the reverse flow below $z/D_c = 1.0$ in comparison with the experiment. This discrepancy could be due to a stronger flow exchange in the experiment, as they use three layers of bed spheres comprising the porous bed, whereas in the LES only one layer of bed spheres is placed below the boulder array as the rough bed. The rest of the computed streamwise velocity profiles agree fairly well with those of the experiment. Figure 3 allows the comparison of the streamwise turbulence intensity between the LES and the experiment at the same locations as in Figure 2. The streamwise turbulence intensities of profiles $0 D_x$ to $4 D_x$ attain their local maximum around the elevation of the boulder crest due to the shear-layer and flow separation from the boulder and the turbulence structures evolving as a result of these. From $5 D_x$ to $9 D_x$, the maximum streamwise turbulence intensity is found near the rough bed, a result of boundary layer recovery, and hence, the flow behaves more like the flow over a rough bed (Bai et al., 2013; Stoesser, 2010). The predicted profiles are generally in reasonably good agreement with the measured data.

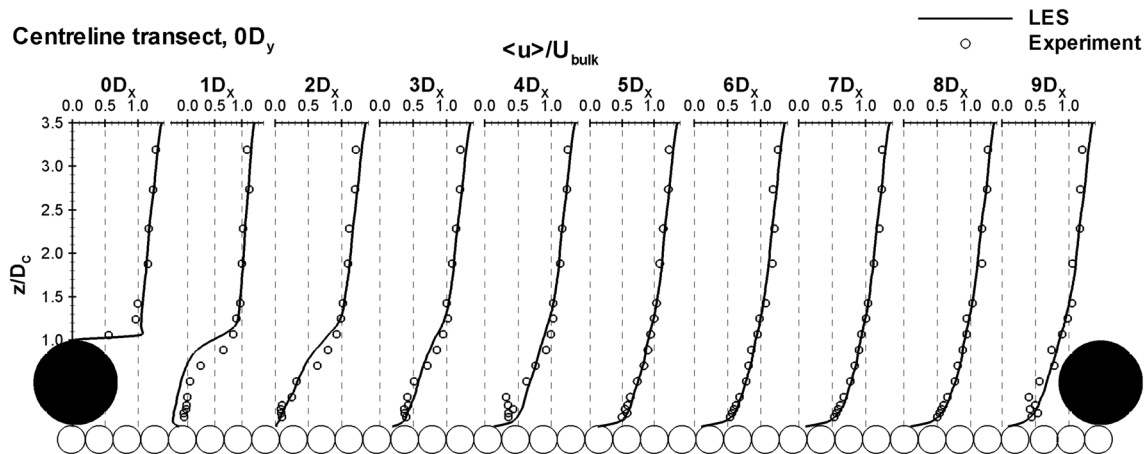


Figure 2. Profiles of the normalized streamwise velocity at the centerline transect.

3.2. Effect of Boulder Concentration on the Local Flow Field

The presence of a boulder causes flow deceleration downstream and upstream, recirculation, and formation of a wake. The deceleration of the flow as a function of boulder concentration is quantified via a streamwise velocity defect, defined as the difference in streamwise velocity between the nonboulder simulation and the with-boulder ($\lambda = 10 D_c$, $5 D_c$, and $2 D_c$) simulations, Δu , below $z/D_c = 0.9$, as suggested by Dey et al. (2011), who concluded that the boulder’s effects on the streamwise velocity profiles are noticeable below $z/D_c = 0.9$. For a given x and z , the maximum value of Δu , Δu_{max} , is chosen as an indicator of the deceleration due to the presence of the boulder.

Figure 4 presents the longitudinal distribution of Δu_{max} along the centerline of the boulder for the three cases with boulders. For the large boulder spacing ($10 D_c$), the velocity reduction is found from $1 D_c$ upstream of the boulder to $5 D_c$ downstream of the boulder and this fits well the boundary layer recovery mentioned above. From $5 D_x$ to $9 D_x$, Δu_{max} is negligibly small, and therefore, the boulder has no impact on the near-bed streamwise velocity suggesting that the boundary layer has (nearly) fully recovered. The peak of Δu_{max} is found at $1 D_x$ with a value of approximately $0.95 U_{bulk}$, which coincides with the location of flow reattachment. Boundary layer recovery occurs rapidly downstream as Δu_{max} decreases exponentially. Studies of flow over spheres (Dey et al., 2011; Papanicolaou et al., 2012) have suggested a near-wake zone and a far-wake zone downstream of the spheres. The near-wake zone is defined as the zone where the flow reverses direction and the far-wake zone is defined as the zone where there is deceleration near the bed (Papanicolaou et al., 2012). Within the framework of the near-wake and far-wake definitions, the length of the entire wake zone in our study extends to $5 D_c$ which is in accordance with the results of Dey et al. (2011), who observed a

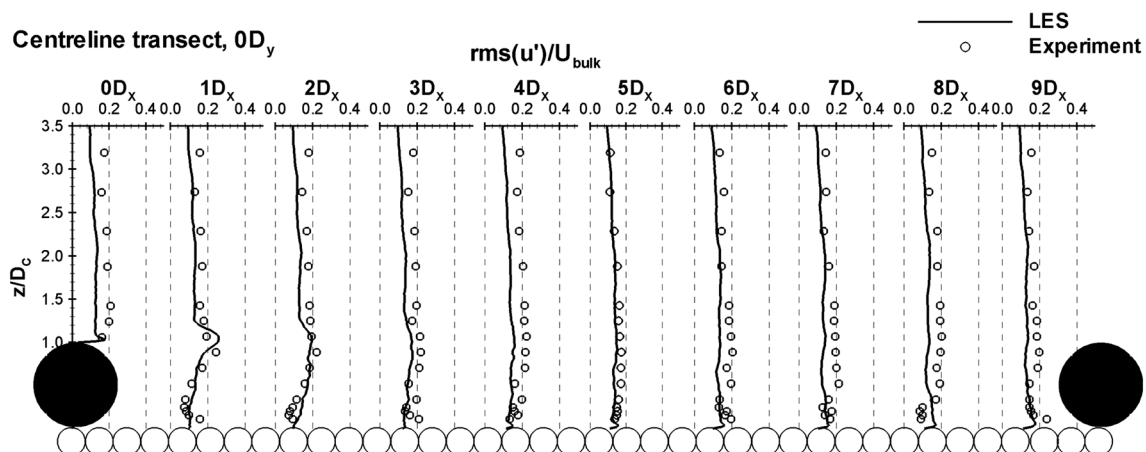


Figure 3. Profiles of the normalized streamwise turbulent intensity at centerline transect.

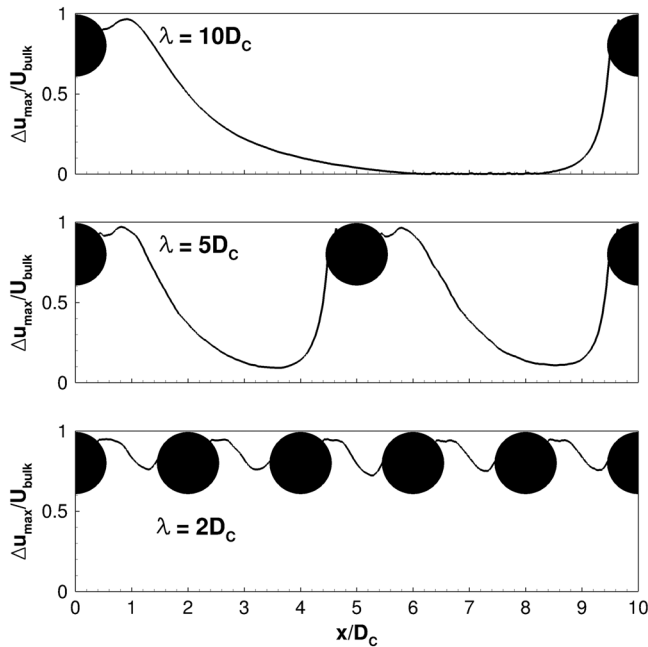


Figure 4. Near-bed flow reduction profiles along the centerline of boulder arrays at $0 D_y$ transect.

far-wake extending from $1.5 D_c$ to $5 D_c$ downstream of a fully submerged single sphere. Noteworthy is the fact that the boulder also decelerates the near-bed flow upstream; however, the extent, approximately $1 D_c$, is much smaller than the one downstream, i.e., $5 D_c$. For the medium spacing ($5 D_c$), a velocity deficit is found at all locations of the centerline transect. The Δu_{max} profile reaches a minimum at $4 D_c$ downstream of the boulder. From $0 D_c$ to $4 D_c$, the deficit is due to the wake of the upstream boulder, whereas between $4 D_c$ and $5 D_c$ the deficit is due to the flow approaching the next boulder.

For the small-spacing simulation ($2 D_c$), the velocity deficit is significant at all locations, with Δu_{max} ranging from 0.75 to $0.95 U_{bulk}$. The peak value of Δu_{max} is approximately the same as the peak values in the $10 D_c$ and $5 D_c$ spacing simulations; however, the location of the peak is shifted slightly toward the upstream, located near the edge of the boulder. The wake flow and hence the boundary layer recovery is disturbed continuously by downstream boulders, and the flow is considered in the wake interference regime, probably close to the skimming regime.

Figure 5 plots 3-D streamlines downstream of the boulder together with contours of the time-averaged vertical velocity in the center plane for the three flows with different boulder-to-boulder spacings. The streamlines in large-spacing simulation and medium-spacing simulation are similar, with a funnel vortex downstream of the boulder. The funnel vortex

is largest near the bed and is limited in the vertical by the downwash of fluid that passes over the crest of the boulder and as evidenced by the blue contours in the $0 D_y$ transect. There are some appreciable differences between the flow over the small-spaced boulders and the medium- and large-spaced boulder flows. First of all, the recirculation-vortex of the small-spacing simulation is significant smaller than that of medium- and large-spacing simulations and the vortex is not clearly defined, or in other words, the funnel vortex is less coherent. Second, the downwash of fluid over the small-spaced boulder is less pronounced than that of its medium- and large-spaced equivalent because the downstream boulder obstructs the downwash. Third, spanwise entrainment of fluid appears to be of lesser significance the closer the boulders are together. These differences between the flows over the small-spaced boulder in comparison with the wider-spaced boulders suggest that the former is a wake interference or even skimming flow.

3.3. Effect of Boulder Concentration on the Near-Bed Shear Stress

The reach-averaged total shear stress τ_t is calculated via equation (17). The τ_t of the no-boulder simulation is $\tau_{t0} = 3.01 \text{ pa}$, and it is used to nondimensionalize the shear stresses of the other simulations. Thus, a dimensionless shear stress that is greater than 1.0 indicates that the shear stress is enhanced by the presence of

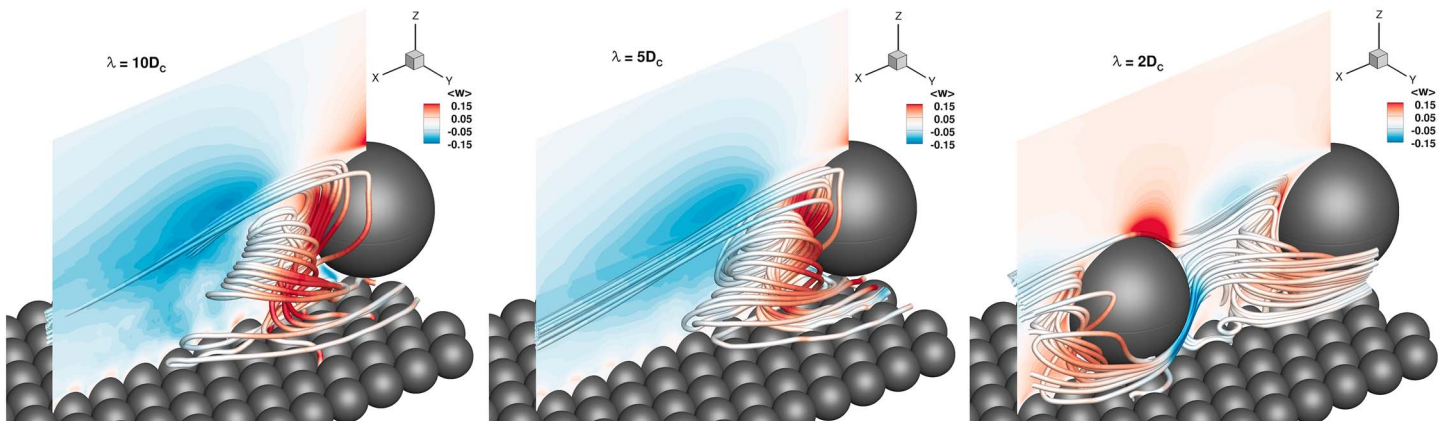


Figure 5. 3-D streamlines downstream of the boulder for the simulations with different boulder spacing.

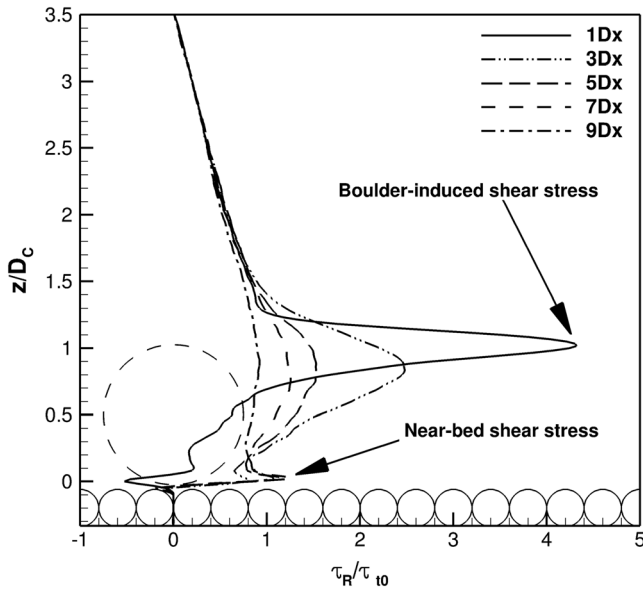


Figure 6. Vertical profiles of the Reynolds shear stresses at selected streamwise locations ($1 D_x$, $3 D_x$, $5 D_x$, $7 D_x$, and $9 D_x$) in the centerline transect.

boulders. Figure 6 plots the vertical dimensionless Reynolds shear stress profiles $\tau_R = -\rho \langle u'w' \rangle$ at selected locations along the centerline ($1 D_x$, $3 D_x$, $5 D_x$, $7 D_x$, and $9 D_x$) of the $10 D_c$ -spacing simulation. An area of high shear stress generated by flow separation and vortex shedding at the boulder crest is observed. The shear stress is noticeable in the profiles from $1 D_x$ to $5 D_x$. The highest value of the shear stress is observed at $1 D_x$ at the elevation of the boulder crest with a dimensionless value of 4.5. Meanwhile, a secondary peak is found near the rough bed at approximately $z/D_c = 0.1$ for all the profiles. The secondary Reynolds shear stress peak is the skin shear stress on the boulder spheres (bed-sediment particles), i.e., $\tau_{ml} = \tau_{RI}$.

Figure 7 presents longitudinal profiles of the dimensionless local skin shear stress τ_{ml}/τ_{t0} along the centerline of the boulder at $z/D_c = 0.1$ for all four simulations. The no-boulder simulation yields a constant τ_{ml} distribution. Small local fluctuations of the skin shear stress τ_{ml} are due to the bed spheres. The dimensionless skin shear stress τ_{ml}/τ_{t0} near the bed is approximately 0.97, supporting the method of replacing the local skin shear stress τ_{ml} with the Reynolds shear stress τ_R at $z/D_c = 0.1$. The distribution of τ_{ml} of the $10 D_c$ -spacing simulation is approximately the same as that of the no-boulder simulation from approximately $5 D_x$ to $9 D_x$. When

approaching the boulder, τ_{ml}/τ_{t0} first slightly decreases to 0.67 due to upstream deceleration of the flow, and then increases sharply to 2.26 due to the horseshoe vortices generated upstream of the boulder. It is noteworthy that the high shear stress region is limited to within a length of $0.5 D_c$ upstream of the boulder. This indicates that the horseshoe vortices are only present in a small area just beneath the big boulder. Downstream, in the wake of the boulder, the minimum skin shear stress is found just downstream of the boulder at $0.5 D_c$ with a value of $\tau_{ml}/\tau_{t0} = 0.5$. The skin shear stress is clearly reduced in the near-wake of the boulder until $5 D_x$. The longitudinal profile of τ_{ml}/τ_{t0} of the $5 D_c$ -spacing simulation

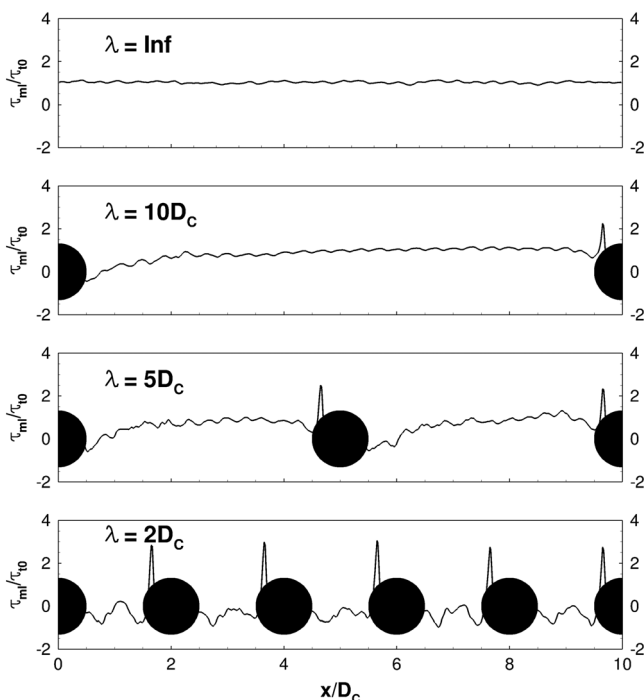


Figure 7. Profiles of the near-bed shear stress along the centerline of the boulders.

is similar to the profile of the $10 D_c$ spacing, i.e., reduction of the skin shear stress in the near-wake, a constant value outside of the near-wake, reduction due to upstream flow deceleration, and increase due to horseshoe vortices very close to the upstream side of the boulder. The τ_{ml}/τ_{t0} in the $2 D_c$ -spacing simulation remains negative at all the locations, suggesting reverse flow, except for some local flow acceleration just upstream of the boulder. The maximum shear stress caused by the upstream horseshoe vortices is approximately $\tau_{ml}/\tau_{t0} = 3.0$, which is higher than the maximum value in the large-spacing simulation. The skin shear stress at the other locations ranges from $\tau_{ml}/\tau_{t0} = -1.3$ to 0. In the negative shear-stress region, sediment has the opportunity to deposit, whereas in the area of peak shear stresses, erosion is likely to occur.

In addition to the quantification of the local dimensionless shear stress in the streamwise direction, the distribution over the entire domain is visualized. Figure 8 presents contours of the normalized difference of skin shear stress between with-boulder simulations and the no-boulder simulation, $\Delta\tau_{ml}/\tau_{t0}$, in a horizontal plane at $z/D_c = 0.1$. The high shear-stress region induced by horseshoe vortices is obvious, and they are limited to just upstream of the boulder. The low shear-stress regions in the near-wake of the small-spacing simulation are greater than the respective regions of the medium- and large-spacing simulations. In addition, a wide area of enhanced shear-stress is observed in the lateral gaps between boulders for all with-boulder simulations. Noteworthy is the fact that the $5 D_c$ simulation appears to feature the highest shear stresses of all the cases.

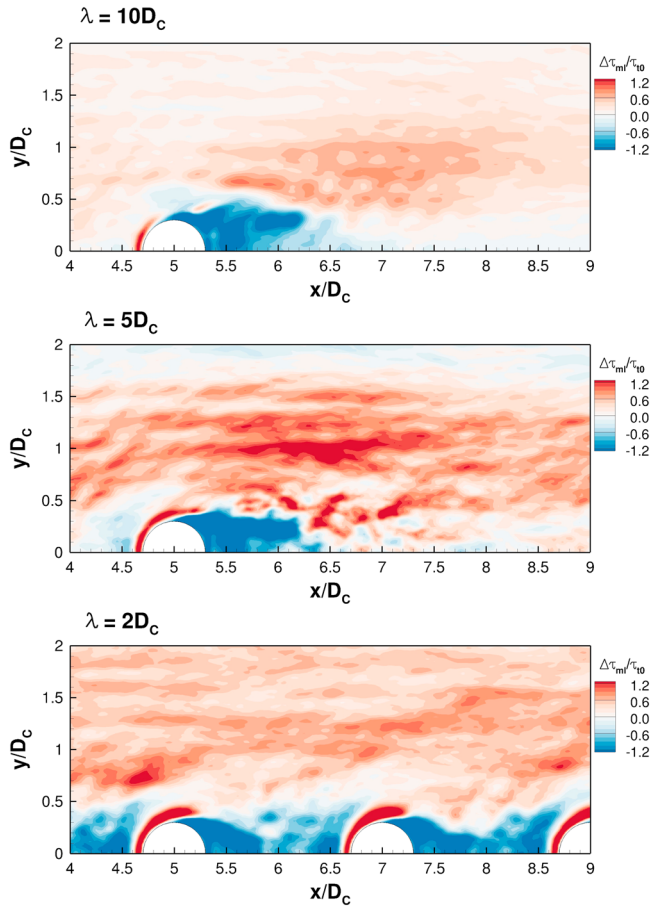


Figure 8. Contours of the near-bed shear stress deficits, $\Delta\tau_m/\tau_{t0}$, for the simulations with (top) $\lambda = 10 D_c$, (middle) $5 D_c$, (bottom) $2 D_c$.

The probability distribution function (PDF) of the dimensionless skin shear stress of the four simulations is plotted in Figure 9 together with various normal distribution function curves. Without boulders the dimensionless skin shear stress is distributed in a narrow range of $\tau_m/\tau_{t0} = 0.6\text{--}1.4$ compared with the range of $\tau_m/\tau_{t0} = -1\text{--}2$ for with-boulder simulations. The maximum distribution density is approximately $f(\tau_m/\tau_{t0}) = 4$ at $\tau_m/\tau_{t0} = 1.0$ in the no-boulder simulation, while the maximum distribution density is approximately $f(\tau_m/\tau_{t0}) = 2.0$ at $\tau_m/\tau_{t0} = 1.08$, $f(\tau_m/\tau_{t0}) = 1.9$ at $\tau_m/\tau_{t0} = 1.11$, and $f(\tau_m/\tau_{t0}) = 1.8$ at $\tau_m/\tau_{t0} = 1.32$ (ignoring the peak value at $\tau_m/\tau_{t0} = 0.0$) for the large-, medium-, and small-spacing simulations, respectively. The dimensionless skin shear stress of the area of the bed covered by immobile boulders is 0, i.e., $\tau_m/\tau_{t0} = 0.0$. Therefore, the value of $f(\tau_m/\tau_{t0})$ at $\tau_m/\tau_{t0} = 0.0$ increases with decreasing boulder spacing, due to the fact that there are more boulders occupying the bed. The expectations of the normal distribution function in Figure 9 are $\mu = 1.0, 1.08, 1.11,$ and 1.15 , equaling the behavior of the dimensionless reach-averaged skin shear stress τ_m/τ_{t0} (Figure 10) of the four simulations. The standard deviation σ of the PDF for the no-boulder simulation is 0.1, and it increases to around 0.2 for the three with-boulder simulations. It is shown in Figure 9 that except for the small-spacing simulation, the other three PDFs of τ_m/τ_{t0} are similar to the normal distribution function. For the small-spacing simulation, the normal distribution function does not properly describe the PDF of τ_m/τ_{t0} . The location with the maximum $f(\tau_m/\tau_{t0})$ value (ignoring the peak value at $\tau_m/\tau_{t0} = 0.0$) is at $\tau_m/\tau_{t0} = 1.32$, which is higher than the expectation of $\mu = 1.15$. The shift is caused by a larger $f(\tau_m/\tau_{t0})$ distribution in the region from $\tau_m/\tau_{t0} = -1$ to 0.4, where the probability density of the normal probability function is around 0.

Figure 10 plots for all the simulations, the dimensionless reach-averaged total shear stress τ_t/τ_{t0} , and the dimensionless reach-averaged grain shear stress τ_m/τ_{t0} as a function of total number of boulders in the domain, with the purpose of quantifying the impact of the boulder arrays on the reach-averaged shear stress. The reach-averaged dimensionless grain shear stress τ_m/τ_{t0} for $N_B = 0, 2, 4,$ and 10 is 1.0, 1.08, 1.11, and 1.15, respectively, while the reach-averaged dimensionless total shear stress τ_t/τ_{t0} is 1.0, 1.90, 3.00, and 3.26, respectively. Therefore, the reach-averaged dimensionless boulder shear stress (or form drag) τ_B/τ_{t0} is computed as $\tau_B/\tau_{t0} = (\tau_t/\tau_{t0}) - (\tau_m/\tau_{t0})$. The values are $\tau_B/\tau_{t0} = 0.0, 0.82, 1.89,$ and 2.11 for the four runs, or drag of each boulder of $(\tau_B/\tau_{t0})/N_B = 0.41, 0.47,$ and 0.21 for $10 D_c, 5 D_c,$ and $2 D_c$ spacing simulations, respectively. In the large-spacing and medium-spacing simulations, $(\tau_B/\tau_{t0})/N_B$ is approximately double of the small-spacing simulation. This is due to the fact that the small-spacing flow is in the wake interference/skimming flow while the other flows are isolated roughness flows. As shown in Figures 4 and 5, a low-velocity area forms between boulders and the recirculation vortex is confined; hence, downstream boulders are shielded by upstream boulders and will not experience the same fluid drag than the boulders in the isolated roughness regime.

3.4. Effect of Boulder Concentration on Near Bed Turbulent Events

Figure 11 presents longitudinal profiles of near-bed $P_{i,H}$ along the centerline of the boulder array for all with-boulder simulations. For the no-boulder simulation, the proportions of the four turbulent events, outward interaction, ejection, inward interaction, and sweep, are 20%, 35%, 15%, and 40%, respectively (not shown here for brevity). The addition of boulders increases the spatial variability in $P_{i,H}$ in the streamwise direction. For the large-spacing and medium-spacing simulations, bursts and sweeps are dominant upstream of the boulder and inward and outward interactions are less frequent. Downstream of the boulder, events of inward and outward interactions are significantly more frequent, and particularly at the downstream edge of the boulder, outward and inward interactions are the most frequent turbulent events, with proportions of 35%

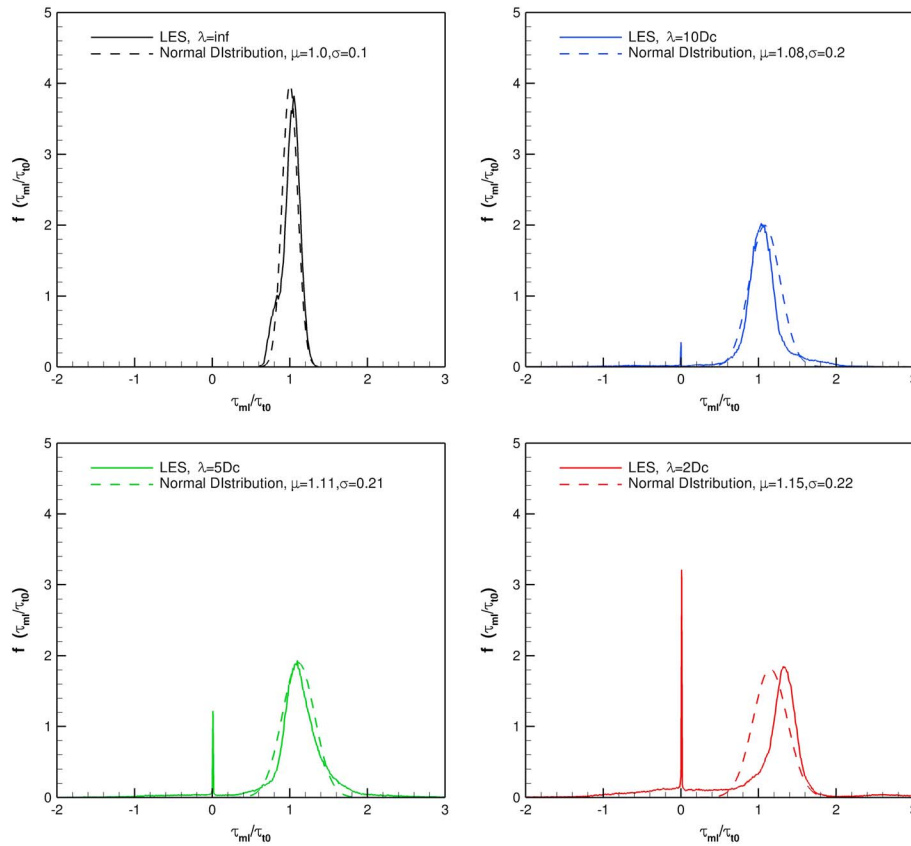


Figure 9. Comparison of τ_{m1}/τ_{10} probability distribution function for all the simulations with the normal probability distribution function.

and 25%, respectively. Further downstream of the boulder, the proportions of bursts and sweeps keep increasing until they reach the proportions for the no-boulder simulations at $5 x/D_c$, which coincides with the length of the boulders' far-wake, or a recovery of the boundary layer.

In the small-spacing simulation, the proportions of turbulent events are very different. Outward and inward interactions are the dominant turbulent events, and bursts and sweeps are suppressed in the entire wake. Outward interactions are the most frequent events from $0.5 x/D_c$ to $1 x/D_c$, while inward interactions become the most frequent event between $1.33 x/D_c$ and $1.5 x/D_c$.

Profiles of the dimensionless turbulent bursting period, Tb^+ , along the boulder's centerline are plotted in Figure 12. Tb^+ in the no-boulder simulation is approximately 96, which is in accordance with the value of $Tb^+ = 100$ reported in other investigations (Luchik & Tiederman, 1987; Willmarth & Sharma, 1984). As expected, the addition of boulders increases significantly the period of near-bed turbulent bursting. The maximum Tb^+ is observed immediately downstream of the boulder, with values of 320, 320, and 390 for $\lambda = 10 D_c$, $5 D_c$ and $2 D_c$ respectively. With increasing distance from the boulder, Tb^+ decreases, as expected. For the large- and medium-spacing simulations, an immediate increase of Tb^+ is observed from $1.5 D_c$ to $2 D_c$ but is not observed for the small-spacing simulation. This is due to the flow reattachment at $2 D_c$ in the large- and medium-spacing simulations. Upstream of flow reattachment, fluid is entrained toward upstream and upward (due to the recirculation), whereas

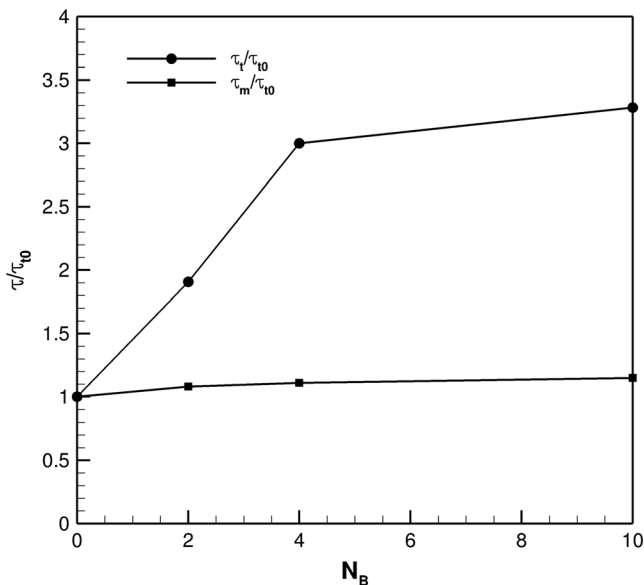


Figure 10. Reach-averaged shear stress distribution for flows different boulder concentration.

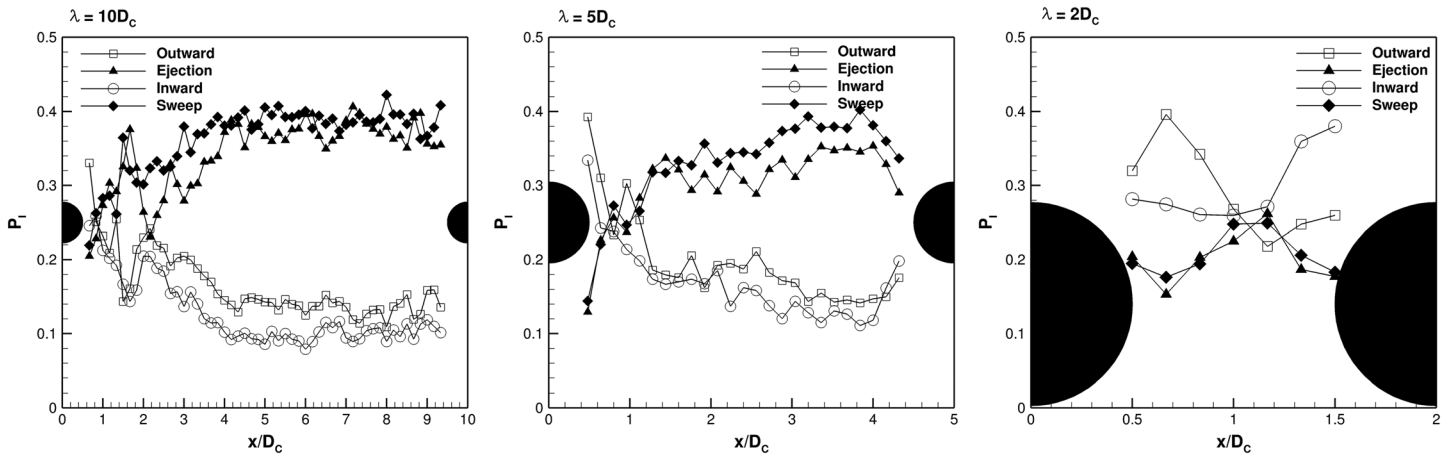


Figure 11. Proportion of the joint turbulent event distribution along the centerline of the boulder arrays.

downstream of the reattachment point, flow is more likely to move toward downstream and upward. Therefore, immediately upstream of the reattachment point, bursts occur more frequently. No flow reattachment takes place in the small-spacing simulation; the secondary peak is absent in the Tb^+ profiles.

3.5. Effect of Boulder Concentration on Sediment Transport Rates

As shown in Figures 7 and 8, the presence of the boulder array decreases the near-bed shear stress in the boulder wake, and at the same time increases the near-bed shear stress immediately upstream and downstream along the sides of the boulder. The dimensionless local bed load transport rate is predicted via equation (14), and it is plotted in the form of q_s^* contours for the three with-boulder simulations in Figure 13. The local dimensionless bed load transport rate corresponds to the near-bed shear stress. The domain may be divided into three regions, i.e., a low (or 0) q_s^* region in the boulder's (near-)wake where local skin shear stress is low, a cambered streak of higher q_s^* streak in the immediate vicinity of the boulder, and an area of increased q_s^* in the corridor between boulders. For the large- and medium spacing simulation, q_s^* is only significantly increased in a limited area about one boulder diameter in the lateral direction and approximately three boulder diameters in the streamwise direction, and this area is observed downstream of the boulder. For the small spacing simulation, increased q_s^* is observed almost in the entire corridor between boulders.

In order to investigate the reach-averaged bed load transport rate q_s^* of the four simulations equations (8) and (12) are employed to calculate the reach-averaged q_{1s}^* and q_{2s}^* . Then the local q_s^* is integrated over the entire domain to obtain a reach-averaged q_{3s}^* using equation (13), without considering areas occupied by the immobile boulders, because q_s^* in the area of immobile boulders is 0. The parameters and results of these calculations are provided in Table 3.

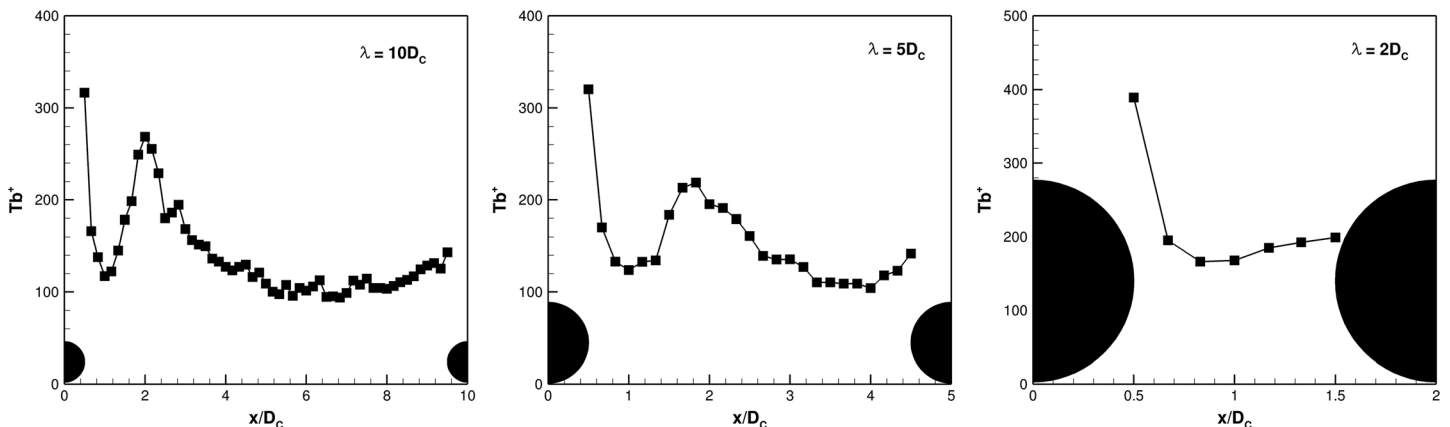


Figure 12. Dimensionless burst period distributions in the $0 D_y$ transect.

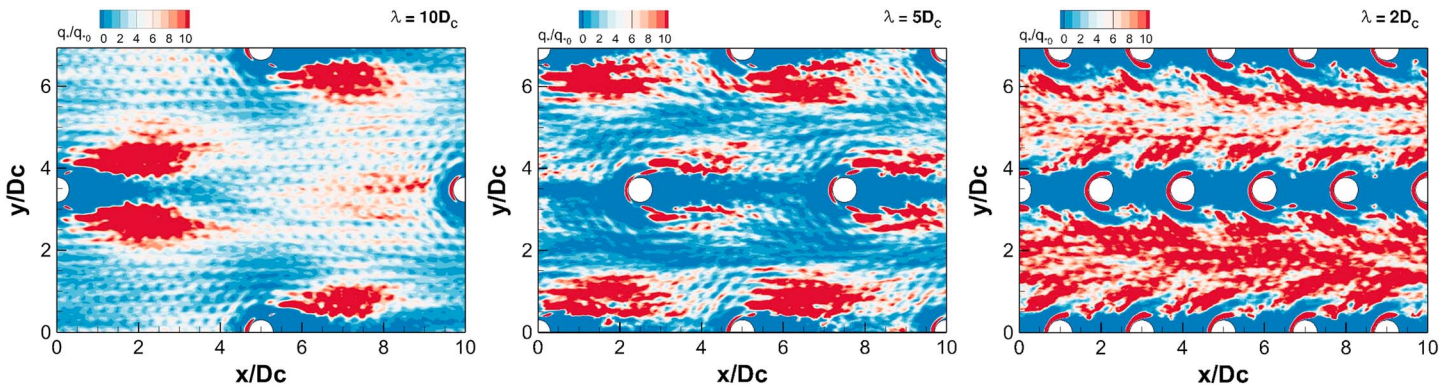


Figure 13. Contours of bed load transport rates for the simulations with $\lambda = 10 D_c$, $5 D_c$, and $2 D_c$.

The boulder spacing influences clearly the reach-averaged bed load transport rates. In terms of q_{1s}^* , bed load transport rate increases with decreasing boulder spacing. The presence of immobile boulders leads to an increase in q_{1s}^* by at least 1 order of magnitude from 2.4×10^{-4} to 5.1×10^{-3} (of the large spacing case). In the medium spacing and small spacing simulations q_{1s}^* attains similar values of approximately 1.2×10^{-2} , which is nearly 50 times of q_{1s}^* without boulders. As for q_{2s}^* , all four simulations yield similar transport rates with $q_{2s}^* = 1.3 \times 10^{-4} - 1.5 \times 10^{-4}$. This is because the reach-averaged grain stress of the four simulations is approximately the same (see Figure 9). In terms of q_{3s}^* , the same increase with decreasing the boulder spacing is observed as for q_{1s}^* ; however, the increase is less significant than that of q_{1s}^* . The presence of immobile boulders increases q_{3s}^* by less than 1 order of magnitude from 1.4×10^{-4} to 5.5×10^{-4} , or approximately by a factor of 3 for the large-spacing case. The maximum increase of q_{3s}^* relative to q_{3s}^* of the no-boulder simulation is approximately by factor 9 for the small spacing case.

The impact of using the local shear stress in comparison with using the reach-averaged shear stress to compute the bed load transport rate is quantified by comparing q_{1s}^* , q_{2s}^* , and q_{3s}^* . The ratio q_{1s}^*/q_{3s}^* and q_{2s}^*/q_{3s}^* are provided in the last two columns of Table 3. In general, compared with the local-variable computed bed load transport rate, q_s^* is overestimated when using the reach-averaged total shear stress in the bed load transport formula, whereas q_s^* is underestimated when using the reach-averaged grain shear stress in the formula. The predicted q_{1s}^*/q_{3s}^* is in the range of 8.4–19.0, which agrees well with other findings that using the total shear stress could overestimate bed load rate by an order of magnitude (e.g., Bathurst, 1987; Yager et al., 2007; Yager & Schmeeckle, 2013). The dimensionless bed load transport rates based on the reach-averaged skin shear stress q_{2s}^* and that based on local near-bed skin shear stress q_{3s}^* are also compared. The predicted values of q_{2s}^*/q_{3s}^* suggest that with decreasing the boulder spacing, the error caused by ignoring the variability of local bed shear stress increases from 10% in the no boulder simulation to 89% in the small spacing simulation. This is reasonable because more boulders will result in a more complicated local shear stress distribution.

4. Discussions

4.1. Local Sediment Transport and Local Flow Turbulence

The areas of low and high bed load transport rates around immobile boulders predicted via high-resolution large-eddy simulations show significant differences in comparison with bed load transport rates around

Table 3
Comparisons of the Reach-Averaged Bed Load Rates Calculated From Equations (8), (12), and (13)

| Runs | λ/D_c | q_{1s}^* Equation (8) | q_{2s}^* Equation (12) | q_{3s}^* Equation (13) | q_{1s}^*/q_{3s}^* | q_{2s}^*/q_{3s}^* |
|----------------|---------------|----------------------------|-----------------------------|-----------------------------|---------------------|---------------------|
| No-boulder | inf | 2.4×10^{-4} | 1.3×10^{-4} | 1.4×10^{-4} | 1.7 | 0.90 |
| Large spacing | 10 | 5.1×10^{-3} | 1.4×10^{-4} | 5.5×10^{-4} | 9.3 | 0.25 |
| Medium spacing | 5 | 1.3×10^{-2} | 1.3×10^{-4} | 7.1×10^{-4} | 19.0 | 0.18 |
| Small spacing | 2 | 1.1×10^{-2} | 1.5×10^{-4} | 1.3×10^{-3} | 8.4 | 0.11 |

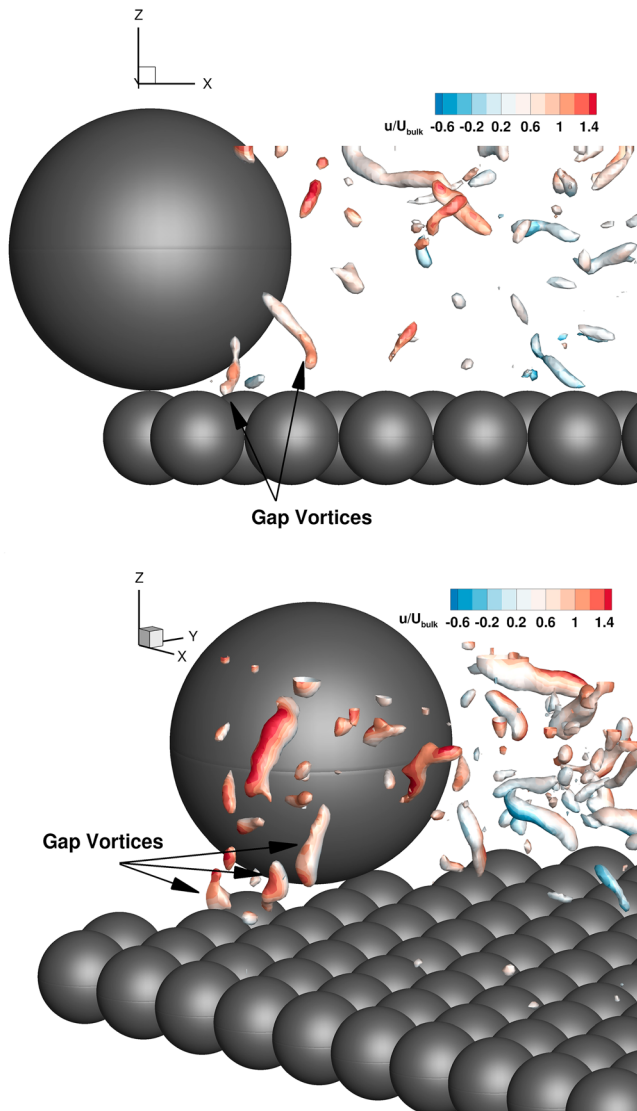


Figure 14. Iso-contours of $Q = 120$ colored by the instantaneous streamwise velocity near the boulder.

cylinders (Radice & Tran, 2012; Yager & Schmeeckle, 2013). Most noteworthy is the low bed load transport rate region in the wake of boulders (Figure 13), whereas both Radice and Tran (2012) and Yager and Schmeeckle (2013) observed high bed load transport rates immediately downstream of cylinders. The results also predict higher bed load transport rates immediately upstream of the boulder, while Yager and Schmeeckle (2013) showed that the bed load transport rate upstream of rigid cylinders is lower than in the wake of the cylinders. There are only very few bed load transport rate data sets available related to flow over immobile boulders; however, investigations of sediment erosion and deposition around submerged spherical and hemispherical large obstacles (Bauri & Sarkar, 2016; Dixen et al., 2013; Shamloo et al., 2001) support, at least qualitatively, the behavior predicted in this study. For example, Shamloo et al. (2001) and Dixen et al. (2013) both observed sediment erosion upstream of and along the sides of submerged hemispheres placed on mobile sediments, including similarly high bed load transport rates as predicted in this study. Shamloo et al. (2001) and Dixen et al. (2013) also observed sediment deposition in the wake of their hemispheres, again in accordance with the LES-predicted low bed load transport behind the boulders. The difference in terms of local sediment transport between flow over submerged boulders and flow around cylinders is the result of different flow fields around the two types of obstacles. One possible reason may be that the submerged boulders enable fast flow in the gap underneath the boulders and above the bed spheres, and thus, relatively high-velocity flow when approaching boulders, and as is shown in Figure, is partially forced to accelerate just above the mobile bed (Figure 5) and this flow acceleration is thought to be responsible for erosion in the immediate vicinity of the boulder/hemisphere, also reported by Shamloo et al. (2001) and Dixen et al. (2013). Another reason may be that some of the experiments mentioned with cylinders (Radice & Tran, 2012; Yager & Schmeeckle, 2013) had deformable beds, whereas the bed in this study is flat, which could produce different shear stress distributions. Also, the relative submergence of the experiment with cylinders (Radice & Tran, 2012; Yager & Schmeeckle, 2013) is different to this numerical study, which may influence the detailed flow structure around the submerged obstacles. The near-bed flow in the boulders' wakes of this study is distinctly 3-D, while it could be argued that the most energetic flow behind a long cylinder is quasi-two-dimensional.

It is demonstrated that the spatial variability in sediment transport around obstacles correlates with near-bed variations in flow turbulence (Nelson et al., 1995). The presence of the boulder alters the local near-bed shear stress in three main areas (Figure 8): immediately upstream of the boulder with a high near-bed stress due to horseshoe vortices, in the boulder wake with a low near-bed stress due to the velocity deficit and at the transverse sides of the boulder with high near-bed stress due to local flow acceleration underneath the boulder. As the predicted bed load transport is solely based on the local near-bed shear stress, the local bed load rate is subsequently increased or decreased, according to the local near bed shear stress.

The effect of boulder concentration is also seen in the behavior of near-bed turbulent events in the vicinity of the boulder. Sweeps and bursts are more important upstream of the boulder, and inward and outward interactions are prominent immediately downstream. Yager and Schmeeckle (2013) also found increased inward and outward interactions in the wake of cylinders. The inward and outward interactions downstream of the boulder may be due to highly local vertical flow (Stoesser et al., 2009). Bursts are the main turbulent events that entrain sediment (Cao, 1997). The increase of the burst period in the wake of the boulder may be partially responsible for the sediment deposition in the wake reported by other researchers (Dixen et al., 2013; Papanicolaou et al., 2012; Shamloo et al., 2001). Significant coherent vortex structures are generated in the

gap between the lower boulder surface and the bed-sphere crest (Figure 14). The so-called gap vortices are transported downstream and away from the bed in the vertical direction. They may be responsible for the high Reynolds shear-stress region just underneath the boulder and above the bed spheres. These near-bed coherent structures have been reported to have a high capability of entraining suspended sediment (Zedler & Street, 2001).

4.2. Bed Load Transport Rates Based on Reach-Scale Parameters and Local Parameters

Three different definitions of the shear stress are employed to predict the bed load transport rates, i.e., reach-scale total shear stress, reach-scale skin shear stress, and local skin shear stress. The results show that the bed load transport rate is overestimated when using the reach-scale total shear stress q_{1s}^* in comparison with the bed load transport rate based on the local skin shear stress q_{3s}^* , while the bed load transport rate is underestimated when using the reach-scale skin shear stress q_{2s}^* in comparison with q_{3s}^* . Both the overestimation and underestimation increases with decreasing boulder spacing. By applying equations (8), (12), and (13), it is shown that the local bed load transport rate is exponentially correlated to the near-bed shear stress with a power of 1.5. Therefore, using the reach-averaged total/skin shear stress will induce magnified errors due to ignoring the variance of the local near-bed shear stress. These errors increase with decreasing boulder spacing because of increased local velocity/shear stress variability in the smaller-spacing simulations. It is demonstrated in this study that a more detailed local distribution of skin shear stress is needed to enable reliable sediment transport predictions in flows over large boulders placed on a mobile bed.

The present results show that in simulations with low boulder concentration (no-boulder, $10 D_c$ spacing, and $5 D_c$ spacing), the local bed shear stress can be approximated by a normal distribution function. The expectation of the normal distribution equals the reach-averaged skin shear stress. The standard deviation of the normal distribution increases with decreasing boulder spacing, but more simulations should be carried out to parameterize the relationship of the standard deviation with flow conditions other than the ones used here, such as relative submergence, varying boulder size, and varying discharge. The normal distribution of bed shear stress is valid when assuming that the combination of turbulent ejections and sweeps causes equally effective grain shear stresses in both upstream and downstream directions (Kleinhans & Rijn, 2002). There are also numerically obtained results of the normal distribution of bed shear stress in natural rivers (Monsalve et al., 2016). For the low boulder concentrations, the near bed turbulent events are only interrupted in the wake zone of boulders, which occupies only a small proportion of the total bed area (Figure 11). Therefore, the PDF follows a normal distribution. However, with the small boulder spacing, the PDF of the near-bed shear stress no longer follows a normal distribution but has a higher density in the region of $\tau_{ml}/\tau_{t0} > 1$. This agrees with the field observations of Segura and Pitlick (2015), who observed that 54–58% of the bed area in the river experiences local shear stress higher than the reach-averaged shear stress.

4.3. Impact of Boulder Spacing on Sediment Transport

It is found that the streamwise spacing may be more important in identifying the flow regimes instead of using the boulder concentration as a parameter. The flow over the small-spaced boulders is shown to be in the wake-interference or skimming regime, and this is supported by the following evidence: (1) streamwise flow velocity in the region of $z/D_c < 0.9$ never recovers to a boundary layer of flow over rough bed (Figure 4) and (2) 3-D streamlines downstream of the boulder exhibit significant differences to the equivalent of medium- and large-spacing simulations (Figure 5) and (3) the reach-averaged total shear stress can no longer be given as the sum of single boulders (Figure 10). Similar findings have been reported by other researchers (Canovaro et al., 2007; Papanicolaou et al., 2001; Papanicolaou et al., 2002). The boulder concentration of the small spacing simulation is $\Gamma = 11.33\%$, which is apparently lower than the one in Ferro (1999) and Papanicolaou et al. (2001), i.e., $\Gamma = 50\%$, or Canovaro et al. (2007) $\Gamma = 30\%$. However, the boulder concentration includes both the streamwise and the spanwise spacing of boulders; in the present simulation the spanwise spacing is quite large; hence, the concentration is comparatively low. In natural rivers, the ratio of the streamwise spacing to the spanwise spacing may vary greatly depending on the various channel types (e.g., cascade and step-pool). It seems that the boulder concentration may not be an ideal parameter to distinguish between the different flow types; it is shown here that the streamwise boulder spacing appears to be an important parameter too.

Overestimation of the sediment transport rate is a function of the boulder spacing. As per equation (13), the calculation of the sediment transport rate depends largely on the skin shear stress distribution. For large- and medium-spaced boulders, the skin shear stress distribution can be expressed via a normal distribution with standard deviation of approximately 0.2. However, for the small-spaced boulders the normal distribution with a standard deviation of 0.22 underestimates the spatial variability of the skin shear stress distribution. This influences the prediction of sediment transport rates as shown in Table 3, and here presented in the form of the relative difference q_{1s}^*/q_{3s}^* , which is greater in the medium spacing simulation than in the small spacing simulation.

5. Conclusions

The presence of boulder arrays placed on a rough streambed will significantly influence the mean flow, near-bed turbulence, and coherent flow structures. Near bed flow deceleration, quantified by the velocity deficit, is found both upstream and downstream of the boulder. The velocity deficit extends until five boulder diameters downstream, which corresponds to the length of the boulder wake reported by Dey et al. (2011), and spans one boulder diameter upstream. A high near-bed shear stress area is observed, created by the horseshoe vortices and gap vortices generated by local high-velocity flow in the sideways vicinity of the boulder. In contrast, low near-bed shear stresses are found in the boulder wake where the flow velocity is decreased. The frequencies of near bed turbulent events are altered by the boulder; i.e., in the wake ejections and sweeps are suppressed, and hence, inward interaction and outward interaction are enhanced.

The streamwise spacing of the boulder array plays an important role in the flow field upstream and downstream. When the boulder spacing λ is relatively large ($10 D_c$), the maximum near bed velocity deficit reduces to 0 five boulder diameters downstream of the boulder; hence, full boundary layer recovery takes place. However, when λ decreases to $2 D_c$, the maximum near bed velocity deficit is greater than $0.7 U_{bulk}$ for the entire boulder wake and this has a profound effect on the near bed shear stress. The 3-D streamlines in the boulder wake indicate that the vortex of the large- and medium-spacing simulations exhibits a funnel shape while the vortex in the small-spacing simulation is less coherent. All the above features suggest that wake interference or even skimming flow is present for $\lambda = 2 D_c$ while the two other configurations yield isolated roughness flows.

The shear stress distributions are different depending on the flow regimes: (1) a normal distribution is a good approximation of the shear stress distribution of the flows in isolated roughness regime but does not fit well in the wake interference flow case and (2) the reach-averaged total shear stress is linearly correlated with the number of boulders in the isolated flow regime but rather exponential in the wake interference flow regime.

In terms of the sediment transport rate predictions, low bed load transport rates are predicted in the wake of the boulder, due to relatively low shear stress and less frequent burst events there. In contrast, high bed load transport rates are predicted immediately upstream of the boulder due to horseshoe vortices. When considering the reach scale, predicted bed load transport rates will increase with decreasing boulder spacing λ , because of an increase in local turbulence. The use of the reach-averaged total shear stress in the bed load rate prediction equation will result in overprediction of bed load transport rates by up to 25 times compared with predictions using local skin shear stress. The use of reach-averaged skin shear stress will result in an underprediction of 11%. This highlights the importance of considering the local shear-stress distribution to accurately predict the bed load transport rate in flows over boulder arrays.

Acknowledgments

This research is supported by the National Natural Science Foundation of China (91647210) and Key Research and Development Program of China (2016YFC0402506). Yan Liu is funded by the CSC (China Scholarship Council). The computations were supported by THPCC (Tsinghua High-performance Computing Center). All the data in this study are produced by the in-house code, Hydro3D. The data are available from the website (<http://www.lifangti-sediment.com/paper-resource/liuy/>).

References

- Bai, J., Fang, H., & Stoesser, T. (2013). Transport and deposition of fine sediment in open channels with different aspect ratios. *Earth Surface Processes and Landforms*, 38(6), 591–600. <https://doi.org/10.1002/esp.3304>
- Bathurst, J. C. (1987). Critical conditions for bed material movement in steep, boulder-bed streams. *International Association of Hydrological Sciences Publication*, 165, 309–318.
- Bathurst, J. C. (2007). Effect of coarse surface layer on bed-load transport. *Journal of Hydraulic Engineering*, 133(11), 1192–1205. [https://doi.org/10.1061/\(ASCE\)0733-9429\(2007\)133:11\(1192\)](https://doi.org/10.1061/(ASCE)0733-9429(2007)133:11(1192))
- Bathurst, J. C., Simons, D. B., & Li, R. M. (1981). Resistance equation for large-scale roughness. *Journal of the Hydraulics Division*, 107(12), 1593–1613.
- Bauri, K. P., & Sarkar, A. (2016). Flow and scour around vertical submerged structures. *Sādhanā*, 41(9), 1039–1053.
- Bomminayuni, S., & Stoesser, T. (2011). Turbulence statistics in an open-channel flow over a rough bed. *Journal of Hydraulic Engineering*, 137(11), 1347–1358. [https://doi.org/10.1061/\(ASCE\)HY.1943-7900.0000454](https://doi.org/10.1061/(ASCE)HY.1943-7900.0000454)

- Buffington, J. M., & Montgomery, D. R. (1997). A systematic analysis of eight decades of incipient motion studies, with special reference to gravel-bedded rivers. *Water Resources Research*, 33(8), 1993–2029. <https://doi.org/10.1029/96WR03190>
- Byrd, T. C., Furbish, D. J., & Warburton, J. (2000). Estimating depth-averaged velocities in rough channels. *Earth Surface Processes and Landforms*, 25(2), 167–173. [https://doi.org/10.1002/\(SICI\)1096-9837\(200002\)25:2%3C167::AID-ESP66%3E3.3.CO;2-7](https://doi.org/10.1002/(SICI)1096-9837(200002)25:2%3C167::AID-ESP66%3E3.3.CO;2-7)
- Canovaro, F., Paris, E., & Solari, L. (2007). Effects of macro-scale bed roughness geometry on flow resistance. *Water Resources Research*, 43(10), W10414. <https://doi.org/10.1029/2006WR005727>
- Cao, Z. (1997). Turbulent bursting-based sediment entrainment function. *Journal of Hydraulic Engineering*, 123(3), 233–236. [https://doi.org/10.1061/\(ASCE\)0733-9429\(1997\)123:3\(233\)](https://doi.org/10.1061/(ASCE)0733-9429(1997)123:3(233))
- Cevheri, M., McSherry, R., & Stoesser, T. (2016). A local mesh refinement approach for large-eddy simulations of turbulent flows. *International Journal for Numerical Methods in Fluids*, 82(5), 261–285. <https://doi.org/10.1002/flid.4217>
- Dey, S., Sarkar, S., Bose, S. K., Tait, S., & Castro-Orgaz, O. (2011). Wall-wake flows downstream of a sphere placed on a plane rough wall. *Journal of Hydraulic Engineering*, 137(10), 1173–1189. [https://doi.org/10.1061/\(ASCE\)HY.1943-7900.0000441](https://doi.org/10.1061/(ASCE)HY.1943-7900.0000441)
- Dixen, M., Sumer, B. M., & Fredsøe, J. (2013). Numerical and experimental investigation of flow and scour around a half-buried sphere. *Coastal Engineering*, 73(7), 84–105. <https://doi.org/10.1016/j.coastaleng.2012.10.006>
- Ferguson, R. I. (2003). The missing dimension: Effects of lateral variation on 1-D calculations of fluvial bedload transport. *Geomorphology*, 56(1–2), 1–14. [https://doi.org/10.1016/S0169-555X\(03\)00042-4](https://doi.org/10.1016/S0169-555X(03)00042-4)
- Fernandez Luque, R., & Van Beek, R. (1976). Erosion and transport of bed-load sediment. *Journal of Hydraulic Research*, 14(2), 127–144. <https://doi.org/10.1080/00221687609499677>
- Ferro, V. (1999). Friction factor for gravel-bed channel with high boulder concentration. *Journal of Hydraulic Engineering*, 125(7), 771–778. [https://doi.org/10.1061/\(ASCE\)0733-9429\(1999\)125:7\(771\)](https://doi.org/10.1061/(ASCE)0733-9429(1999)125:7(771))
- Ferro, V. (2003). ADV measurements of velocity distributions in a gravel-bed flume. *Earth Surface Processes and Landforms*, 28(7), 707–722. <https://doi.org/10.1002/esp.467>
- Fraga Bugallo, B., & Stoesser, T. (2016). Influence of bubble size, diffuser width and flow rate on the integral behavior of bubble plumes. *Journal of Geophysical Research: Oceans*, 121, 3887–3904. <https://doi.org/10.1002/2015JC011381>
- Fraga Bugallo, B., Stoesser, T., Lai, C., & Socolofsky, S. (2016). A large-eddy simulation-based Eulerian-Lagrangian approach to predict bubble plume dynamics. *Ocean Modelling*, 97(2016), 27–36. <https://doi.org/10.1016/j.ocemod.2015.11.005>
- Ghilardi, T., Franca, M. J., & Schleiss, A. J. (2014). Bulk velocity measurements by video analysis of dye tracer in a macro-rough channel. *Measurement Science and Technology*, 25(3), 035003. <https://doi.org/10.1088/0957-0233/25/3/035003>
- Hajimirzaie, S. M., Tsakiris, A. G., Buchholz, J. H., & Papanicolaou, A. N. (2014). Flow characteristics around a wall-mounted spherical obstacle in a thin boundary layer. *Experiments in Fluids*, 55(6), 1–14. <https://doi.org/10.1007/s00348-014-1762-0>
- Kara, S., Stoesser, T., & Sturm, T. W. (2012). Turbulence statistics in compound channels with deep and shallow overbank flows. *Journal of Hydraulic Research*, 50(5), 482–493. <https://doi.org/10.1080/00221686.2012.724194>
- Kara, M. C., Stoesser, T., & McSherry, R. (2015). Calculation of fluid structure interaction: Methods, refinements, applications. *Proceedings ICE - Engineering Computers Mechanisms*, 168(2), 59–78.
- Kara, S., Stoesser, T., & Sturm, T. W. (2015). Free-surface versus rigid-lid LES computations for bridge-abutment flow. *Journal of Hydraulic Engineering*, 141(9), 04015019. [https://doi.org/10.1061/\(ASCE\)HY.1943-7900.0001028](https://doi.org/10.1061/(ASCE)HY.1943-7900.0001028)
- Kara, S., Stoesser, T., Sturm, T. W., & Mulahasan, S. (2015). Flow dynamics through a submerged bridge opening with overtopping. *Journal of Hydraulic Research*, 53(2), 186–195. <https://doi.org/10.1080/00221686.2014.967821>
- Kim, S. J., & Stoesser, T. (2011). Closure modeling and direct simulation of vegetation drag in flow through emergent vegetation. *Water Resources Research*, 47(10), W10511. <https://doi.org/10.1029/2011WR010561>
- Kim, D., Stoesser, T., & Kim, J. H. (2013). The effect of baffle spacing on hydrodynamics and solute transport in serpentine contact tanks. *Journal of Hydraulic Research*, 51(5), 558–568. <https://doi.org/10.1080/00221686.2013.777681>
- Kleinhans, M. G., & Rijn, L. C. V. (2002). Stochastic prediction of sediment transport in sand-gravel bed rivers. *Journal of Hydraulic Engineering*, 128(4), 412–425. [https://doi.org/10.1061/\(ASCE\)0733-9429\(2002\)128:4\(412\)](https://doi.org/10.1061/(ASCE)0733-9429(2002)128:4(412))
- Lamb, M. P., Dietrich, W. E., & Venditti, J. G. (2008). Is the critical Shields stress for incipient sediment motion dependent on channel-bed slope? *Journal of Geophysical Research*, 113, F02008. <https://doi.org/10.1029/2007JF000831>
- Lenzi, M. A., Mao, L., & Comiti, F. (2006). When does bedload transport begin in steep boulder-bed streams? *Hydrological Processes*, 20(16), 3517–3533. <https://doi.org/10.1002/hyp.6168>
- Liu, Y., Stoesser, T., Fang, H., Papanicolaou, A., & Tsakiris, A. (2017). Turbulent flow over an array of boulders placed on a rough, permeable bed. *Computers & Fluids*, 158, 120–132. <https://doi.org/10.1016/j.compfluid.2017.05.023>
- Luchik, T. S., & Tiederman, W. G. (1987). Timescale and structure of ejections and bursts in turbulent channel flows. *Journal of Fluid Mechanics*, 174, 529–552. <https://doi.org/10.1017/S0022112087000235>
- Mao, L., Uyttendaele, G. P., Iroumé, A., & Lenzi, M. A. (2008). Field based analysis of sediment entrainment in two high gradient streams located in alpine and andine environments. *Geomorphology*, 93(3–4), 368–383. <https://doi.org/10.1016/j.geomorph.2007.03.008>
- Monsalve, A., Yager, E. M., Turowski, J. M., & Rickenmann, D. (2016). A probabilistic formulation of bed load transport to include spatial variability of flow and surface grain size distributions. *Water Resources Research*, 52(5), 3579–3598. <https://doi.org/10.1002/2015WR017694>
- Nelson, J. M., Shreve, R. L., McLean, S. R., & Drake, T. G. (1995). Role of near-bed turbulence structure in bed load transport and bed form mechanics. *Water Resources Research*, 31(8), 2071–2086. <https://doi.org/10.1029/95WR00976>
- Nicoud, F., & Ducros, F. (1999). Subgrid-scale stress modelling based on the square of the velocity gradient tensor. *Flow, Turbulence and Combustion*, 62(3), 183–200. <https://doi.org/10.1023/A:1009995426001>
- Nitsche, M., Rickenmann, D., Kirchner, J. W., Turowski, J. M., & Badoux, A. (2012). Macroroughness and variations in reach-averaged flow resistance in steep mountain streams. *Water Resources Research*, 48(12), W12518. <https://doi.org/10.1029/2012WR012091>
- Ozgoren, M., Okbaz, A., Dogan, S., Sahin, B., & Akilli, H. (2013). Investigation of flow characteristics around a sphere placed in a boundary layer over a flat plate. *Experimental Thermal and Fluid Science*, 44, 62–74. <https://doi.org/10.1016/j.expthermflusc.2012.05.014>
- Papanicolaou, A. N., Diplas, P., Dancey, C. L., & Balakrishnan, M. (2001). Surface roughness effects in near-bed turbulence: Implications to sediment entrainment. *Journal of Engineering Mechanics*, 127(3), 211–218. [https://doi.org/10.1061/\(ASCE\)0733-9399\(2001\)127:3\(211\)](https://doi.org/10.1061/(ASCE)0733-9399(2001)127:3(211))
- Papanicolaou, A. N., Diplas, P., Evaggelopoulos, N., & Fotopoulos, S. (2002). Stochastic incipient motion criterion for spheres under various bed packing conditions. *Journal of Hydraulic Engineering*, 128(4), 369–380. [https://doi.org/10.1061/\(ASCE\)0733-9429\(2002\)128:4\(369\)](https://doi.org/10.1061/(ASCE)0733-9429(2002)128:4(369))
- Papanicolaou, A. N., Kramer, C. M., Tsakiris, A. G., Stoesser, T., Bomminayuni, S., & Chen, Z. (2012). Effects of a fully submerged boulder within a boulder array on the mean and turbulent flow fields: Implications to bedload transport. *Acta Geophysica*, 60(6), 1502–1546. <https://doi.org/10.2478/s11600-012-0044-6>

- Parker, G. (2008). Transport of gravel and sediment mixtures. *Sedimentation engineering: Processes, measurements, modeling, and practice*, 110, 165–252. <https://doi.org/10.1061/9780784408148.ch03>
- Patel, S. B., Patel, P. L., & Porey, P. D. (2013). Threshold for initiation of motion of unimodal and bimodal sediments. *International Journal of Sediment Research*, 28(1), 24–33. [https://doi.org/10.1016/S1001-6279\(13\)60015-3](https://doi.org/10.1016/S1001-6279(13)60015-3)
- Radice, A., & Tran, C. K. (2012). Study of sediment motion in scour hole of a circular pier. *Journal of Hydraulic Research*, 50(1), 44–51. <https://doi.org/10.1080/00221686.2011.641764>
- Recking, A. (2009). Theoretical development on the effects of changing flow hydraulics on incipient bed load motion. *Water Resources Research*, 45, W04401.
- Rickenmann, D. (2001). Comparison of bed load transport in torrents and gravel bed streams. *Water Resources Research*, 37(12), 3295–3305. <https://doi.org/10.1029/2001WR000319>
- Scheingross, J. S., Winchell, E. W., Lamb, M. P., & Dietrich, W. E. (2013). Influence of bed patchiness, slope, grain hiding, and form drag on gravel mobilization in very steep streams. *Journal of Geophysical Research: Earth Surface*, 118, 982–1001. <https://doi.org/10.1002/jgrf.20067>
- Segura, C., & Pitlick, J. (2015). Coupling fluvial-hydraulic models to predict gravel transport in spatially variable flows. *Journal of Geophysical Research: Earth Surface*, 120, 834–855. <https://doi.org/10.1002/2014JF003302>
- Shamloo, H., Rajaratnam, N., & Katopodis, C. (2001). Hydraulics of simple habitat structures. *Journal of Hydraulic Research*, 39(4), 351–366. <https://doi.org/10.1080/00221680109499840>
- Stoesser, T. (2010). Physically realistic roughness closure scheme to simulate turbulent channel flow over rough beds within the framework of LES. *Journal of Hydraulic Engineering*, 136(10), 812–819. [https://doi.org/10.1061/\(ASCE\)HY.1943-7900.0000236](https://doi.org/10.1061/(ASCE)HY.1943-7900.0000236)
- Stoesser, T., Salvador, G. P., Rodi, W., & Diplas, P. (2009). Large eddy simulation of turbulent flow through submerged vegetation. *Transport in Porous Media*, 78(3), 347–365. <https://doi.org/10.1007/s11242-009-9371-8>
- Strom, K. B., & Papanicolaou, A. N. (2007). ADV measurements around a cluster microform in a shallow mountain stream. *Journal of Hydraulic Engineering*, 133(12), 1379–1389. [https://doi.org/10.1061/\(ASCE\)0733-9429\(2007\)133:12\(1379\)](https://doi.org/10.1061/(ASCE)0733-9429(2007)133:12(1379))
- Strom, K., Papanicolaou, A. N., Evangelopoulos, N., & Odeh, M. (2004). Microforms in gravel bed rivers: Formation, disintegration and effects on bedload transport. *Journal of Hydraulic Engineering*, 130(6), 554–567. [https://doi.org/10.1061/\(ASCE\)0733-9429\(2004\)130:6\(554\)](https://doi.org/10.1061/(ASCE)0733-9429(2004)130:6(554))
- Tsakiris, A. G., Papanicolaou, A. T., Hajimirzaie, S. M., & Buchholz, J. H. (2014). Influence of collective boulder array on the surrounding time-averaged and turbulent flow fields. *Journal of Mountain Science*, 11(6), 1420–1428. <https://doi.org/10.1007/s11629-014-3055-8>
- Tsutsui, T. (2008). Flow around a sphere in a plane turbulent boundary layer. *Journal of Wind Engineering and Industrial Aerodynamics*, 96(6–7), 779–792. <https://doi.org/10.1016/j.jweia.2007.06.031>
- Uhlmann, M. (2005). An immersed boundary method with direct forcing for the simulation of particulate flows. *Journal of Computational Physics*, 209(2), 448–476. <https://doi.org/10.1016/j.jcp.2005.03.017>
- Wiberg, P. L., & Smith, J. D. (1991). Velocity distribution and bed roughness in high-gradient streams. *Water Resources Research*, 27(5), 825–838. <https://doi.org/10.1029/90WR02770>
- Willmarth, W. W., & Sharma, L. K. (1984). Study of turbulent structure with hot wires smaller than the viscous length. *Journal of Fluid Mechanics*, 142, 121–149. <https://doi.org/10.1017/S0022112084001026>
- Xu, H., Lu, J., & Liu, X. (2008). Non-uniform sediment incipient velocity. *International Journal of Sediment Research*, 23(1), 69–75. [https://doi.org/10.1016/S1001-6279\(08\)60006-2](https://doi.org/10.1016/S1001-6279(08)60006-2)
- Yager, E. M., & Schmeeckle, M. W. (2013). The influence of vegetation on turbulence and bed load transport. *Journal of Geophysical Research: Earth Surface*, 118, 1585–1601. <https://doi.org/10.1002/jgrf.20085>
- Yager, E. M., Kirchner, J. W., & Dietrich, W. E. (2007). Calculating bed load transport in steep boulder bed channels. *Water Resources Research*, 43(7), W07418. <https://doi.org/10.1029/2006WR005432>
- Yager, E. M., Dietrich, W. E., Kirchner, J. W., & McArdeell, B. W. (2012). Prediction of sediment transport in step-pool channels. *Water Resources Research*, 48(1), W01541. <https://doi.org/10.1029/2011WR010829>
- Zedler, E. A., & Street, R. L. (2001). Large-eddy simulation of sediment transport: Currents over ripples. *Journal of Hydraulic Engineering*, 127(6), 444–452. [https://doi.org/10.1061/\(ASCE\)0733-9429\(2001\)127:6\(444\)](https://doi.org/10.1061/(ASCE)0733-9429(2001)127:6(444))